• Original Paper •

An Abrupt Rainfall Decrease over the Asian Inland Plateau Region around 1999 and the Possible Underlying Mechanism

Jinling PIAO[1,2], Wen CHEN[*1,2], Ke WEI[1], Yong LIU[1], Hans-F. GRAF[1],

Joong-Bae AHN[3], and Alexander POGORELTSEV[4]

[1]*Center for Monsoon System Research, Institute of Atmospheric Physics, Chinese Academy of Sciences, Beijing* 100190, *China*

[2]*School of Earth Science, University of the Chinese Academy of Sciences, Beijing* 100049, *China*

[3]*Department of Atmospheric Sciences, Pusan National University, Pusan* 609-735, *Korea*

[4]*Russian State Hydrometeorological University, St. Petersburg* 195196, *Russia*

ABSTRACT

A decadal change in summer rainfall in the Asian inland plateau (AIP) region is identified around 1999. This decadal change is characterized by an abrupt decrease in summer rainfall of about 15.7% of the climatological average amount, leading to prolonged drought in the Asian inland plateau region. Both the surface air temperature and potential evapotranspiration in the AIP show a significant increase, while the soil moisture exhibits a decrease, after the late 1990s. Furthermore, the normalized difference vegetation index shows an apparent decreasing trend during 1999–2007. Three different drought indices—the standardized precipitation index, the standardized precipitation evapotranspiration index, and the self-calibrating Palmer drought severity index—present pronounced climate anomalies during 1999–2007, indicating dramatic drought exacerbation in the region after the late 1990s. This decadal change in the summer rainfall may be attributable to a wave-like teleconnection pattern from Western Europe to Asia. A set of model sensitivity experiments suggests that the summer warming sea surface temperature in the North Atlantic could induce this teleconnection pattern over Eurasia, resulting in recent drought in the AIP region.

Key words: Asian inland plateau, summer rainfall, drought, teleconnection pattern, North Atlantic

---

1. Introduction

The Asian inland plateau (AIP) region is located in the East Asian monsoon marginal areas between the middle and the high latitudes and mainly includes Mongolia and part of northern China. This region mainly covers arid regions and semi-arid regions, relevantly including diverse ecosystems such as forests, grasslands, farmlands and deserts. The climate variability in this region is complex, and can have profound impacts on economic and social activities (Yamanaka et al., 2007; Bai et al., 2008; Chen et al., 2009; Mu et al., 2013; Peng et al., 2013; Tao et al., 2015). The transition regions between the climate zones are particularly vulnerable to irretrievable climate changes. Using multi-temporal Landsat images, Tao et al. (2015) pointed out that precipitation is the main contributor to the lake water-level changes in Mongolia. Peng et al. (2013) suggested that the effects of the

anomalies in precipitation seasonality and frequency are important over semi-arid grasslands in Inner Mongolia. On the interannual time scale, the vegetation coverage in Inner Mongolia is also influenced by precipitation changes (Mu et al., 2013). Hence, it is important to conduct more investigations into the long-term precipitation variation as a manifestation of climate change in this region.

Droughts are characterized by relatively long-term large-scale deficits of precipitation, often along with high temperatures, causing damage to agriculture and ecosystems and leading to problems for agricultural production and economics. Using the surface wetness index, the Palmer drought severity index (PDSI) and the retrieval of soil moisture, Ma and Fu (2006) revealed a significant drying trend in the eastern part of Northwest China and the central part of North China since the 1980s. Wei and Wang (2013) indicated that the spatial extent of aridity and drought have increased in northwestern China since the late 1990s due to an increase in evaporation resulting from rising temperature. By bias-correcting CMIP5 projections, Huang et al. (2015) showed

* Corresponding author: Wen CHEN

  Email: cw@post.iap.ac.cn

that half of the global land surface will be classified as dry-land by the end of this century, exacerbating the risk of land degradation and desertification. The spectrum analyses of Bao et al. (2015) highlighted the importance of large-scale climate forcing for drought development. According to their study, the El Niño–Southern Oscillation, Pacific Decadal Os-cillation and North Atlantic Oscillation might be associated with the drought events of the late 1870s to early 1880s, the 1920s, and since the late 1990s, over the eastern Mongolian Plateau.

As an essential factor in forming droughts, the anoma-lies of precipitation over the AIP have received considerable attention (Zhang et al., 2004; Endo et al., 2006; Sato et al., 2007; Zhu and Meng, 2010; Huang et al., 2015). Zhu and Meng (2010) focused on the spatial and temporal variation of precipitation over the middle part of Inner Mongolia dur-ing 1961–2003. According to their work, a significant in-terannual variation of rainfall exists, with a slightly increas-ing trend. Huang et al. (2015) investigated the spatiotem-poral change in the precipitation characteristics over Inner Mongolia during 1960–2012. They suggested that declin-ing precipitation dominates this region, with fewer extreme precipitation events. Using a regional climate model, Sato et al. (2007) studied the rainfall change over Mongolia due to global warming and inferred that more severe droughts would occur against the background of global warming.

Despite all the work mentioned above, there have been few studies focusing on climate variability over the whole AIP, particularly on decadal time scales. For decadal vari-ability, because of its longer time and larger spatial scales, persistent and frequent droughts may lead to protracted disas-ters. In this paper, we inspect the interdecadal and long-term changes of precipitation and droughts over the whole AIP and discuss the possible driving factors in recent decades. The paper is organized as follows: the data and methods used are introduced in section 2; the primary results are presented in section 3; conclusions and a discussion are given in section 4.

2. Datasets and model

The observational data employed in this study include: (1) Monthly mean horizontal and vertical winds, geopotential height and air temperature, provided by the National Cen-ters for Environmental Prediction–National Center for At-mospheric Research (NCEP–NCAR), spanning the period from 1948 to the present (Kalnay et al., 1996), with a hor-izontal resolution of $2.5° \times 2.5°$. Since there are studies indicating defects in the NCEP–NCAR dataset (e.g., Zuo et al., 2013b; Xue et al., 2015), we compared our results with those derived from the ERA-Interim dataset, but with a shorter period. Both showed quite similar results (fig-ures not shown), indicating the robustness of our results. (2) Monthly mean sea surface temperature (SST) datasets from the Met Office Hadley Center (Rayner et al., 2003), with a resolution of $1° \times 1°$, from 1870 to the present.

(3) The NOAA's precipitation reconstruction data over land (PREC/L), with a horizontal resolution of $2.5° \times 2.5°$, from 1948 to the present (Chen et al., 2002). (4) When calcu-lating the standardized precipitation index (SPI), we also use the GPCC precipitation data, with a horizontal resolu-tion of $0.5° \times 0.5°$, extending from 1901 to 2013, provided by NOAA/OAR/ESRL PSD, Boulder, Colorado, USA, from their website http://www.esrl.noaa.gov/psd/. (5) The topo-graphic data are formatted as 16-bit binary integers contain-ing 2160×4320 data values, one for each five minutes of lat-itude and longitude, from the website http://www.ngdc.noaa. gov/mgg/fliers/93mgg01.html. (6) The global maps of monthly self-calibrating PDSI (sc-PDSI) are based on the Climatic Research Unit Time Series (CRU TS) 3.10.01 data (1901–2009), with a horizontal resolution of $0.5° \times 0.5°$ (Van der Schirier et al., 2013). (7) The potential evapotranspiration (PET) is from CRU 3.23, which has a horizontal resolution of $0.5° \times 0.5°$, from 1901–2014. (8) CPC soil moisture data, with a horizontal resolution of $0.5° \times 0.5°$, extending from January 1948 to June 2016, provided by NOAA/OAR/ESRL PSD, Colorado, USA, from the website http://www.esrl.noaa. gov/psd/. (9) The normalized difference vegetation index (NDVI) is the third generation of the Global Inventory Moni-toring and Modeling System (GIMMS) NDVI from NOAA's AVHRR sensors, spanning from July 1981 to November 2013, from the website http://ecocast.arc.nasa.gov/data/pub/ gimms/3g.v0/. After termed into a netCDF file, it has a horizontal resolution of $0.083333° \times 0.083333°$. (10) The standardized precipitation evapotranspiration index (SPEI) is based on the CRU TS 3.23 dataset, with a spatial resolution of $0.5° \times 0.5°$, from 1901 to 2013, and is available from the website http://hdl.handle.net/10261/128892.

NDVI is a satellite-derived vegetation index, closely re-lated to aboveground net primary productivity. It is calculated as

$$NDVI = (NIR - RED)/(NIR + RED),   (1)$$

where NIR and RED represent the amounts of near-infrared and red light reflected by the vegetation, respectively (Run-ning, 1990; Myneni et al., 1995). NDVI varies from -1 to $+1$, with smaller values corresponding to less vegetation. Much work has been done to study the effects of climate change on ecosystems in terms of NDVI (Nemani et al., 2003; Roerink et al., 2003; Zhou et al., 2003; Pettorelli et al., 2005). In turn, the vegetation change can also exert influence on the climate change. Zuo et al. (2011) indicated that the vegeta-tion around the southern Tibetan Plateau positively correlates with summer rainfall over southern China and North China, but negatively correlates with summer rainfall over the Yel-low River valley and western China. Sc-PDSI, SPEI and SPI are indices most commonly used in recent years for quantify-ing drought severity (Zhai et al., 2010; Wang and Chen, 2014; Wang et al., 2014; Huang et al., 2016). Of all the drought in-dices, PDSI is of crucial importance for the development of measuring drought (Palmer, 1965). It is derived from a sim-ple water balance model, based on precipitation and temper-ature, and its value ranges from -4 to 4. Sc-PDSI adjusts the

way PDSI is calculated, addressing the problem that PDSI is incapable of accounting for precipitation variability between locations (Wells et al., 2004). SPI is an index that can be easily calculated based on the precipitation record, ignoring the effects of temperature on droughts (McKee et al., 1993). Based upon precipitation and PET, SPEI takes advantage of both sc-PDSI and SPI (Vicente-Serrano et al., 2010). Both SPEI and SPI range from −1 to 1. In this paper, all of the drought indices introduced above are calculated at the time scale of 12 months.

To study the propagation features of the stationary Rossby waves (R_{wa}), the wave activity flux (Takaya and Nakamura, 2001) is calculated as

$$R_{wa} = \frac{p}{2|\boldsymbol{U}|} \begin{Bmatrix} U(v'^2 - \psi'v'_x) + V(-u'v' + \psi'u'_x) \\ U(-u'v' + \psi'u'_x) + V(u'^2 + \psi'u'_y) \\ \frac{f_0 R_a}{N^2 H_0}[U(v'T' - \psi'T'_x) + V(-u'T' - \psi'T'_y)] \end{Bmatrix},$$
(2)

where $\boldsymbol{U} = (U, V)$, (u', v'), ψ' and T' denote the basic wind velocity, perturbed geostrophic wind velocity, perturbed geostrophic stream function and perturbed air temperature, respectively. R_a, H_0, f_0, N and p stand for gas constant of dry air, scale height, the Coriolis parameter at 45°N, Brunt-Väisälä frequency and pressure normalized by 1000 hPa, respectively. The climatological monthly mean is based on the period 1971–2000.

We also carry out a number of sensitivity experiments to investigate the effects of the SST warming in the North Atlantic on the development of drought over the AIP region with the GFDL atmospheric model version 2.1 (AM2.1). The model employs a finite-volume dynamical core (Lin, 2004), gridded at 2° latitude by 2.5° longitude resolution. In the vertical direction, it adopts a hybrid coordinate and has 24 levels ranging from about 30 m above the surface up to 3 hPa (approximately 40 km). The land model (LM2.1), based on the land dynamics described by Milly and Shmakin (2002), is coupled with AM2.1. A detailed description and evaluation of the model with prescribed SSTs can be found in Anderson et al. (2004) and Delworth et al. (2006).

We adopt the Student's t-test, moving t-test, Lepage test (Lepage, 1971; Liu et al., 2011), and correlation analysis as statistical tools. The interdecadal component is obtained from the 9-yr running mean. We mainly use the Lepage test to identify the significance of interdecadal change. This is a nonparametric two-sample test for significant differences between two samples, which is calculated by reference to the method mentioned in Yonetani and McCabe (1994) and Liu et al. (2011). Using the standardized statistics of Wilcoxon and Ansari-Bradley, the Lepage test statistic [HK, the abbreviation defined by Yonetani and McCabe (1994)] is calculated as:

$$HK = \frac{[W - E(W)]^2}{V(W)} + \frac{[A - E(A)]^2}{V(A)}.$$
(3)

If HK is greater than 5.99, 4.21 or 9.21, the difference is significant at the confidence level of 95%, 90% and 99%, respectively. We assume sample $\boldsymbol{X} = (x_1, x_2, \ldots, x_m)$

and sample $\boldsymbol{Y} = (y_1, y_2, \ldots, y_n)$, which are independent samples of number m and n, respectively. $\boldsymbol{Q}$ consists of the ranked values of the combination of $\boldsymbol{X}$ and $\boldsymbol{Y}$, which is $(x_1, x_2, \ldots, x_m, y_1, y_2, \ldots, y_n)$:

$$\mu_i = \begin{cases} 0, & Q_i \in \boldsymbol{X} \\ 1, & Q_i \in \boldsymbol{Y} \end{cases}.$$
(4)

We can calculate each item in Eq. (3) according to the equations below:

$$W = \sum_{i=1}^{m+n} i\mu_i;$$
(5)

$$E(W) = \frac{m(m+n+1)}{2};$$
(6)

$$V(W) = \frac{mn(m+n+1)}{2};$$
(7)

$$A = \sum_{i=1}^{m} i\mu_i + \sum_{i=m+1}^{m+n} (m+n-i+1)\mu_i.$$
(8)

When $m+n$ is even, we calculate $E(A)$ and $V(A)$ as follows:

$$E(A) = \frac{m(m+n+2)}{4};$$
(9)

$$V(A) = \frac{mn(m+n-2)(m+n+2)}{48(m+n-1)}.$$
(10)

If the sum is odd:

$$E(A) = \frac{m(m+n+1)^2}{4(m+n)};$$
(11)

$$V(A) = \frac{mn(m+n+1)[(m+n)^2+3]}{48(m+n)^2}.$$
(12)

In this paper, sample $\boldsymbol{X}$ is regarded as the rainfall data for nine years previous to year Y_c (ranging from 1957 to 2006, moved at an interval of one year), with sample $\boldsymbol{Y}$ regarded as that for year Y_c and eight years following year Y_c. Both m and n mentioned above are equal to 9. The details of this method can be found in the paper by Liu et al. (2011).

3.   Results

3.1.   *Interdecadal variation of summer precipitation over the AIP*

Figure 1 shows the topographic map of Eurasia and the annual total rainfall. Over the Mongolian Plateau there is a region with annual rainfall less than 400 mm. Hence, the region (41°–49°N, 94°–124°E) is defined as the AIP as in Fig. 1a (rectangular region). It should be noted that the results in this paper are not sensitive to the choice of this plateau area. That is, with a slightly smaller or larger area (even the whole Mongolian plateau), nearly the same results can be achieved (not shown). The AIP lies in the plateau region, northeast of the Tibetan Plateau. It covers Mongolia, part of Northeast China and the northern part of Inner Mongolia of China (Fig. 1a). In regional mean terms, the total annual mean rainfall is about 227 mm. Multiple climate zones exist over the AIP domain, among which the arid and semi-arid zones dominate
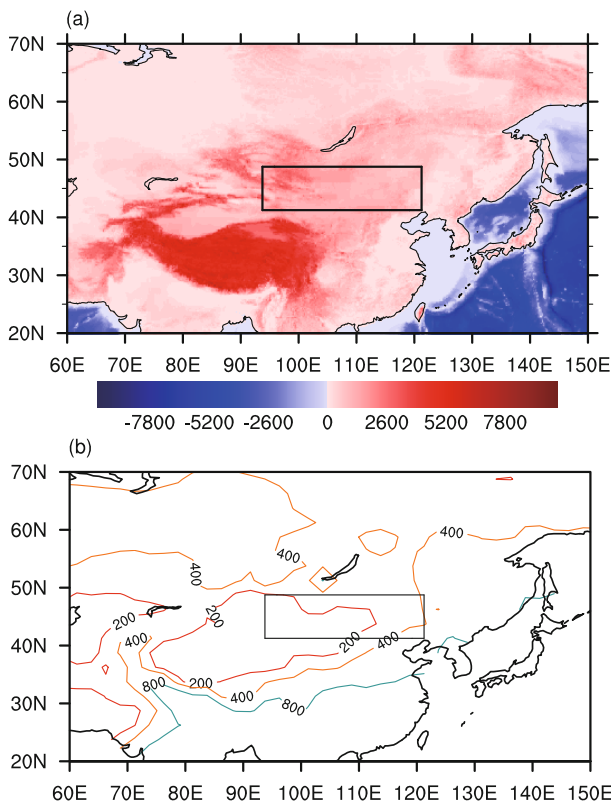
Fig. 1. (a) Topographic map of Eurasia (units: m). (b) Annual rainfall distribution (units: mm). The area within the black box shown in (a) and (b) is the defined AIP region, which is the same as those in Figs. 4–6 and Figs. 8, 10 and 12.

most parts (Fig. 1b). As for the monthly evolution of rainfall (Fig. 2), July and August have much more rainfall than all other months. Indeed, the rainfall amount in these two months accounts for nearly 51% of the total annual amount, whereas the rainfall in January, February, November and December is relatively small. As precipitation over the AIP during July and August contributes most to the total annual rainfall, the average of July and August is regarded as the summer

mean in this study.

Figure 3a exhibits the time series of the regional mean annual rainfall over the AIP, accompanied by their decadal components, which are obtained by removing the period shorter than nine years. The annual rainfall is characterized by both interannual and interdecadal variations. For the interdecadal part, there is a rainfall increase between the late 1940s and the mid-1960s. From the late 1960s to the late 1970s, the interdecadal variation is small. Then, during the mid-1980s to the mid-1990s, there is another increase in rainfall. However, since the late 1990s, the rainfall undergoes a pronounced decrease. The Lepage test (Fig. 3c) indicates that the decrease in 1999 is statistically significant above the 0.1 level. The annual rainfall over the AIP averaged between 1971 and 2000 is about 230 mm, but during 1999–2007 the value is only 194 mm. The rainfall decreases about 15% around 1999. Broadening or narrowing the region of defined as the AIP, the results are similar (figures not shown), indicating the robustness of the rainfall change over the AIP region. In the case of summer (July and August) precipitation, the situation is quite similar. The summer rainfall presents positive anomalies during the 1990s and negative anomalies since the late 1990s (Fig. 3b). According to the Lepage test (Fig. 3d), the value in 1999 is also statistically significant above the 0.1 level. The climatological mean of summer rainfall is about 119 mm. However, during 1999–2007, the amount is about 88 mm, which accounts for only 74% of the climatological mean. It is therefore inferred that, around 1998/99, a decadal change in the precipitation over the AIP appears, with anomalies shifting from positive to negative values.

The intensity of AIP's summer precipitation is estimated with an index defined as the regional mean summer precipitation over the domain of the AIP. To better depict the discrepancies among the different time periods, we regard 1990–98 as T1, 1999–2007 as T2, and the climatology period 1971–2000 as TClim. Figure 4 illustrates the summer precipitation differences between T2 and TClim. Negative anomalies are mainly located over the AIP and the northern part of India, with positive anomalies over the southeastern parts of Kaza-
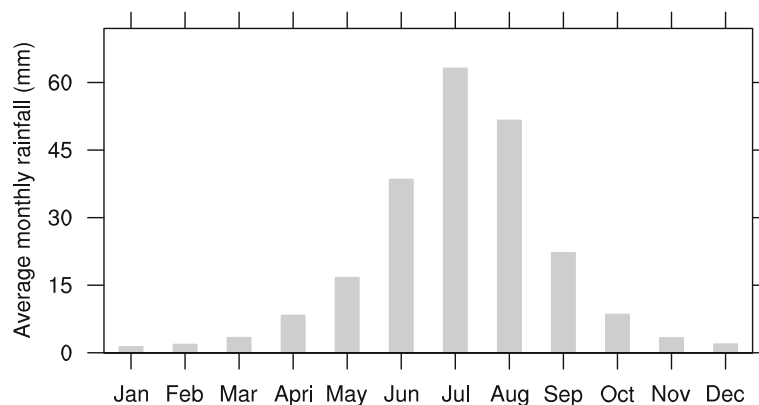

Fig. 2. Monthly precipitation over the AIP region averaged between 1948 and 2013, based on the PREC/L dataset.
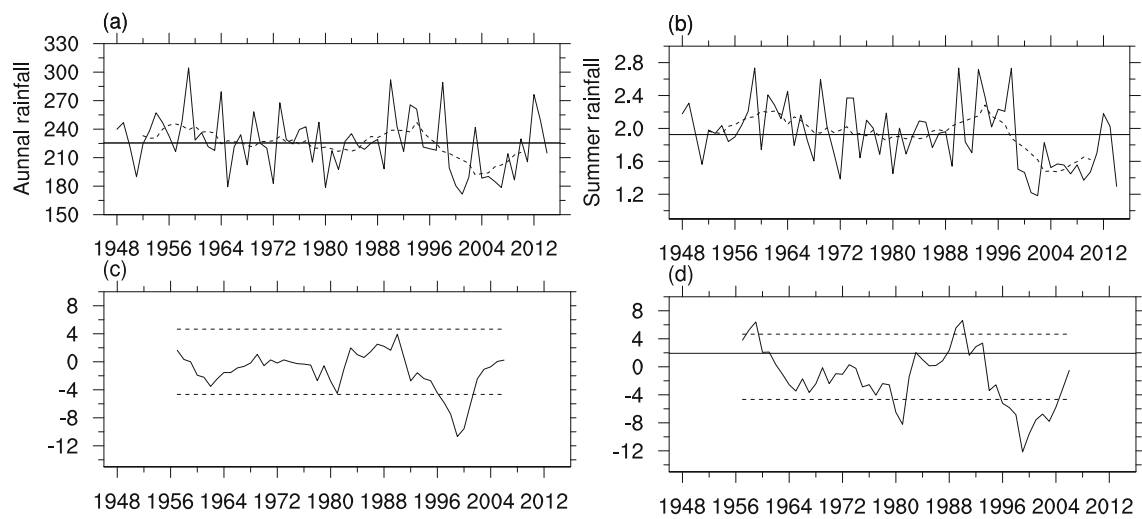
Fig. 3. (a) Time series of regional mean annual rainfall over the AIP (solid line), and the corresponding interdecadal component (dashed line) calculated by removing the period shorter than nine years (units: mm). (b) As in (a), but for the precipitation averaged between July and August. (c, d) Lepage test results calculated using the time series of (a, b), respectively. Values larger than 4.21 (upper dashed line) or smaller than −4.21 (lower dashed line) denote that the difference over nine years prior to and from the corresponding year is significant beyond the 90% confidence level.

khstan and the Yangtze River valley. The anomalies within the AIP are significant at the 10% level, based on the Student's *t*-test (Fig. 4). There have been many investigations on the interannual and decadal summer precipitation change over China. For example, using the Lepage test, Liu et al. (2011) analyzed the interdecadal changes of summer rainfall over East China and found four interdecadal abrupt changes around 1979, 1983, 1993 and 1999. They found an abrupt shift around 1999, with a significant rainfall decrease in summer over North China and Northeast China. Our study confirms their results. Furthermore, we indicate that this abrupt shift happens in a larger area, covering the AIP. Zhu and Meng (2010) focused on the decadal changes of the summer rainfall over East China and suggested an increase in the Huanghe River–Huaihe River region during 2000–08 in comparison to 1979–99. Xu et al. (2015) mentioned different decadal variation features of the summer precipitation from north to south over China after the late 1990s, with decreasing precipitation over Northeast and North China, the lower–middle reaches of the Yangtze River, and South and southwestern China after 1999, but increasing precipitation over southern parts of the Hetao region and Huaihe River valley after 2003. These changes can also be seen in Fig. 4. However, they are only robust over the AIP.

Since precipitation plays a crucial role in the drought condition, the decrease in rainfall after the late 1990s significantly influences the regional drought situation over the AIP. However, the aridity/humidity change in a specific location is determined by evaporation, which is related to temperature and wind, as well as precipitation. Wang et al. (2003) studied the drought condition over northern China from 1950 to 2000 and revealed that the drought area tended to increase and a drought condition rapidly developed. They also mentioned that if the drought problem is associated with global
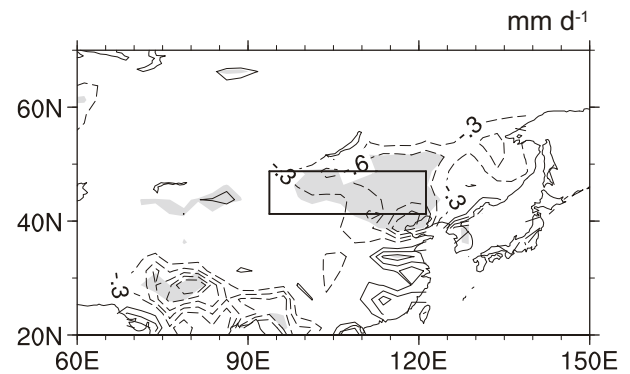

Fig. 4. Summer mean precipitation difference between 1999–2007 (T2) and 1971–2000 (TClim). The contour internal is 0.3 mm d^{-1}. The solid and dashed lines represent positive and negative values, respectively. The shaded areas are where the difference is significant above the 90% confidence level, based on the Student's *t*-test.

warming, the trend will exist in the future. Zou et al. (2005) indicated that the dry area in Northeast, North and eastern Northwest China has increased since the late 1990s, threatening ecosystems and agriculture. Chen and Sun (2015) also demonstrated that the frequency and severity of droughts have both been exacerbated since the late 1990s, especially in the northern part of China. Enlightened by their study, we adopt surface air temperature, PET, soil moisture and NDVI to investigate the variation of aridity. Compared with TClim, the anomalies of surface air temperature and PET appear to be positive over the AIP during T2 (Figs. 5a and b), and soil moisture is decreasing (Fig. 5c). Apart from these parameters, NDVI presents weak negative anomalies, indicating reduced vegetation coverage (Fig. 5d). These results reflect that the drought condition over the AIP is getting worse and im-
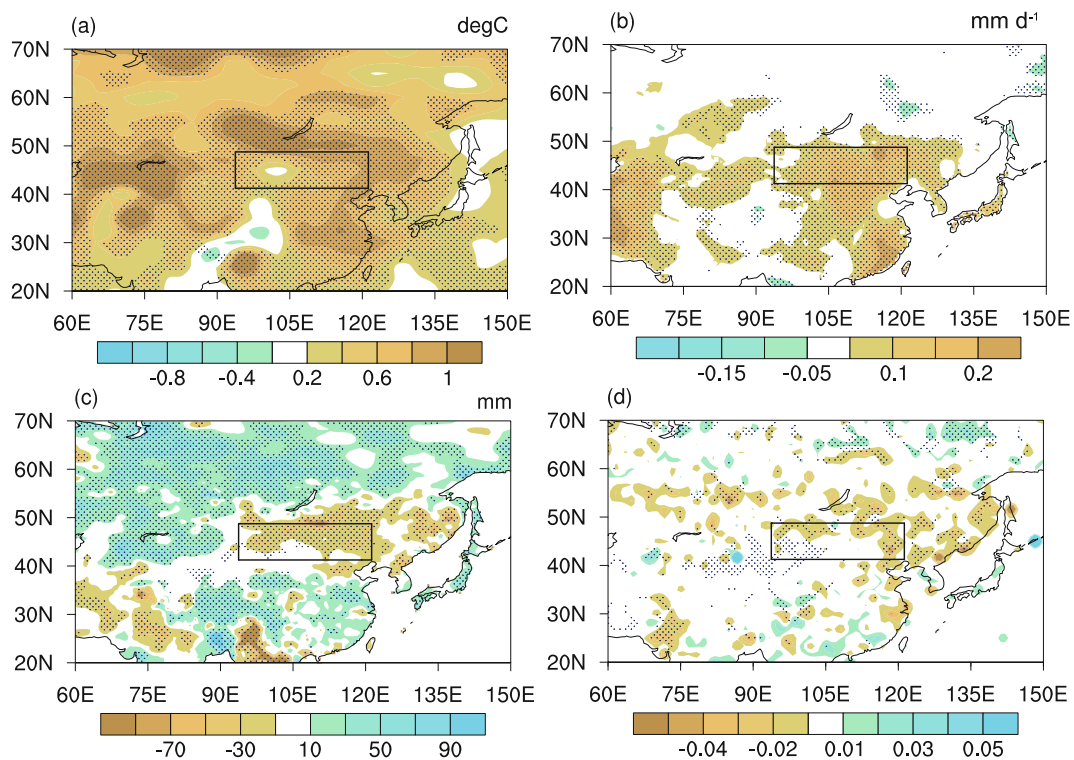
Fig. 5. Difference in (a) surface air temperature (units: °C), (b) PET (units: mm d^{-1}), and (c) soil moisture (units: mm), between 1999–2007 (T2) and 1971–2000 (TClim), and (d) NDVI between 1999–2007 (T2) and 1990–1998 (T1). The dotted regions indicate the 90% confidence level, based on the Student's *t*-test.

pacts ecosystems. Among these four parameters, the negative anomalies of NDVI might result from the drought development, but might also be a factor leading to the deterioration of the drought condition. The relationship between the change in NDVI values and the drought condition is not clear, necessitating further investigations. To lend additional support to this result, three drought indices (sc-PDSI, SPI and SPEI) are adopted to represent the evolution of drought. Sc-PDSI exhibits pronounced negative anomalies over the AIP, north of India, the western part of Pakistan and Afghanistan, coupled with positive anomalies over Central Asia, Siberia and the eastern part of Russia (Fig. 6a). The results for SPEI and SPI are similar to those of sc-PDSI (Figs. 6b and c), except that the anomalies of SPEI and SPI are a little weaker, which is due to the different standards of choosing values. As mentioned before, sc-PDSI ranges from −4 to 4, while SPEI and SPI both range from −1 to 1. Figure 6d further depicts the differences between SPEI and SPI. Over the AIP, the anomalies are significantly negative, which means that the drought condition is aggravated not only by the decrease in precipitation but also the increase in temperature. The time series of regional mean indices for the AIP agree well with the above analysis (Fig. 7). The evolution of the three indices is quite in phase. Around 1999, all of the three indices shift from positive to negative, among which the sc-PDSI shows the biggest change. The absolute values of SPEI after 1999 are larger than those of SPI, indicating the important role of the temperature increase in the development of the drought condition over the AIP.

3.2. *Atmospheric circulation anomalies*

Figure 8 shows the differences of horizontal wind at 850 hPa between T2 and TClim. Anticyclonic anomalies exist over Eastern Europe and the AIP. Cyclonic anomalies exist over Western Europe and Central Asia around Uzbekistan. Over the AIP region, the wind speed decreases during T2 compared to that of TClim (figures not shown). Considering the PET increase during T2 (Fig. 5b), it is inferred that the positive anomalies of the temperature during T2 (Fig. 5a) contribute most to the strengthening of the PET over the AIP. In terms of geopotential height at 200 hPa, 500 hPa and 850 hPa, Fig. 9 presents a wave-like pattern across Eurasia throughout the whole troposphere, with a stronger signal in the upper troposphere. The pattern shown in Fig. 9a exhibits a quasi-zonal wave-like pattern, with positive geopotential anomalies located over Eastern Europe and the AIP, and negative anomalies over Western Europe and Central Asia. The geopotential anomaly distributions at different levels are similar, indicating an equivalent barotropic structure of this wave-like pattern.

It is generally recognized that the teleconnection pattern may induce climate change in different regions (Chen et al., 2003; Zhu et al., 2011; Chen and Huang, 2012; Liu et al., 2014; Xu et al., 2015). Using regression analysis, Chen and Huang (2012) suggested that the Silk Road pattern and Europe–China pattern could contribute to the variations of the leading modes of July precipitation over Northwest China. For the decadal variation of precipitation over eastern China during the late 1990s, Huang et al. (2013) found
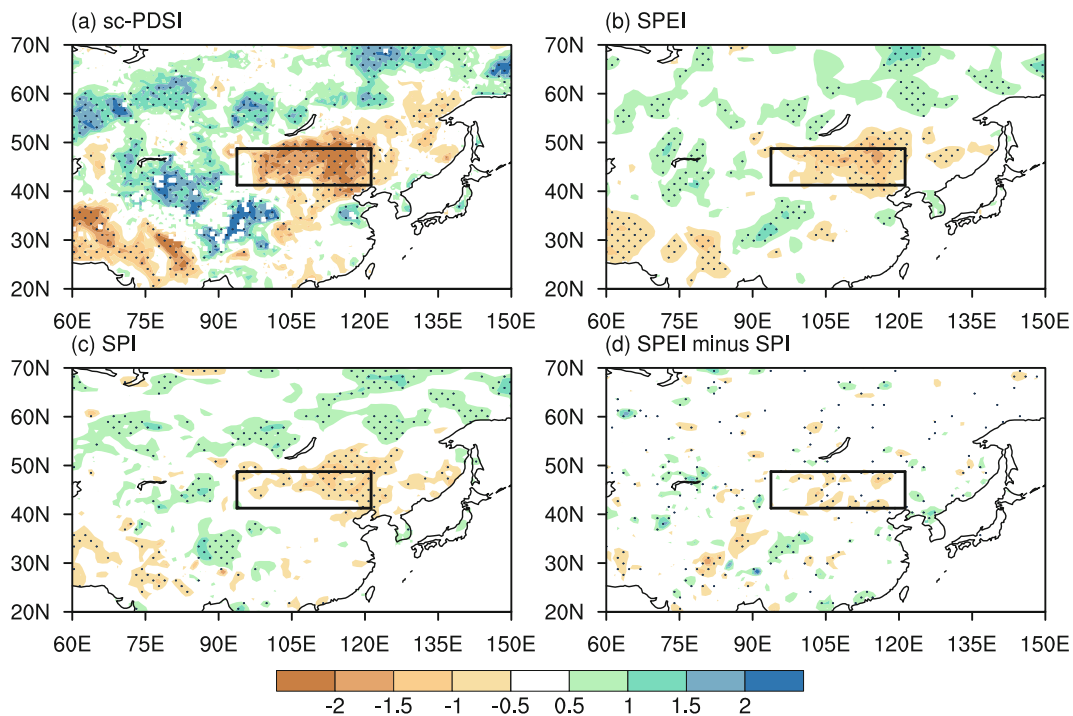
Fig. 6. Difference in (a) sc-PDSI, (b) SPEI, (c) SPI, and (d) SPEI minus SPI, between 1999–2007 (T2) and 1971–2000 (TClim). The dotted areas are where the difference is significant above the 90% confidence level, based on the Student's *t*-test.
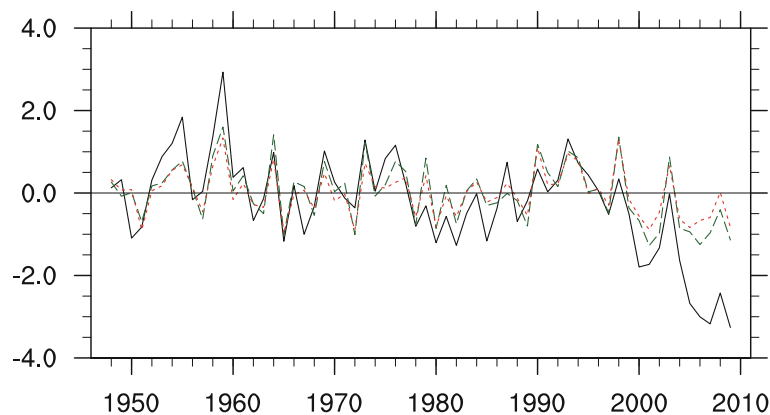

Fig. 7. Time series of area-mean sc-PDSI (black line), SPEI (green line) and SPI (red line).

that the Silk Road pattern, the East Asia–Pacific pattern and Eurasian pattern may all contribute. It is also inferred that the Eurasian pattern-like teleconnection may impose an impact on the decadal rainfall variation around 2003 by changing the atmospheric circulation over Eurasia (Xu et al., 2015). Figure 10a shows the anomalies of the wave activity flux at 200 hPa, derived by the mean of T1 minus TClim. Weak signals are noticed during this period, while during 1999–2007 wave propagation is clearly found over Eurasia (Fig. 10b). The wave propagates quasi-zonally from Western Europe to the AIP. Therefore, this teleconnection pattern, together with the anticyclone over the AIP, is suggested to be responsible for the decrease in summer AIP precipitation.

In the above analysis, we mainly focus on the influences of the teleconnection pattern over Eurasia on the interdecadal variation of summer rainfall over the AIP. On the other hand, according to Fig. 8, the southwesterly winds appear to be weakened during T2 compared with TClim, which is a sign of the weakening of the East Asian summer monsoon (EASM). The weakened summer monsoon could lead to reduced water vapor transport into inland regions, causing the rainfall deficit. There have been many studies pointing out the decadal decrease in the EASM in the late 1990s (Huang et al., 2013; Zuo et al., 2013b; Zhu et al., 2011, 2016; Xu et al., 2015). Here, we employ three EASM indices reflecting the anomalies of the EASM: (1) $EASM_{WF}$, defined as
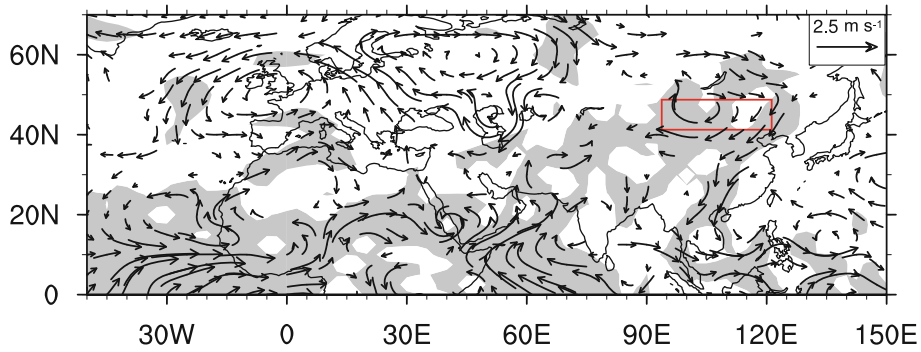
Fig. 8. Differences in horizontal wind at 850 hPa between 1999–2007 (T2) and 1971–2000 (TClim). Gray shading represents the region statistically significant above the 90% confidence level, based on the Student's *t*-test.
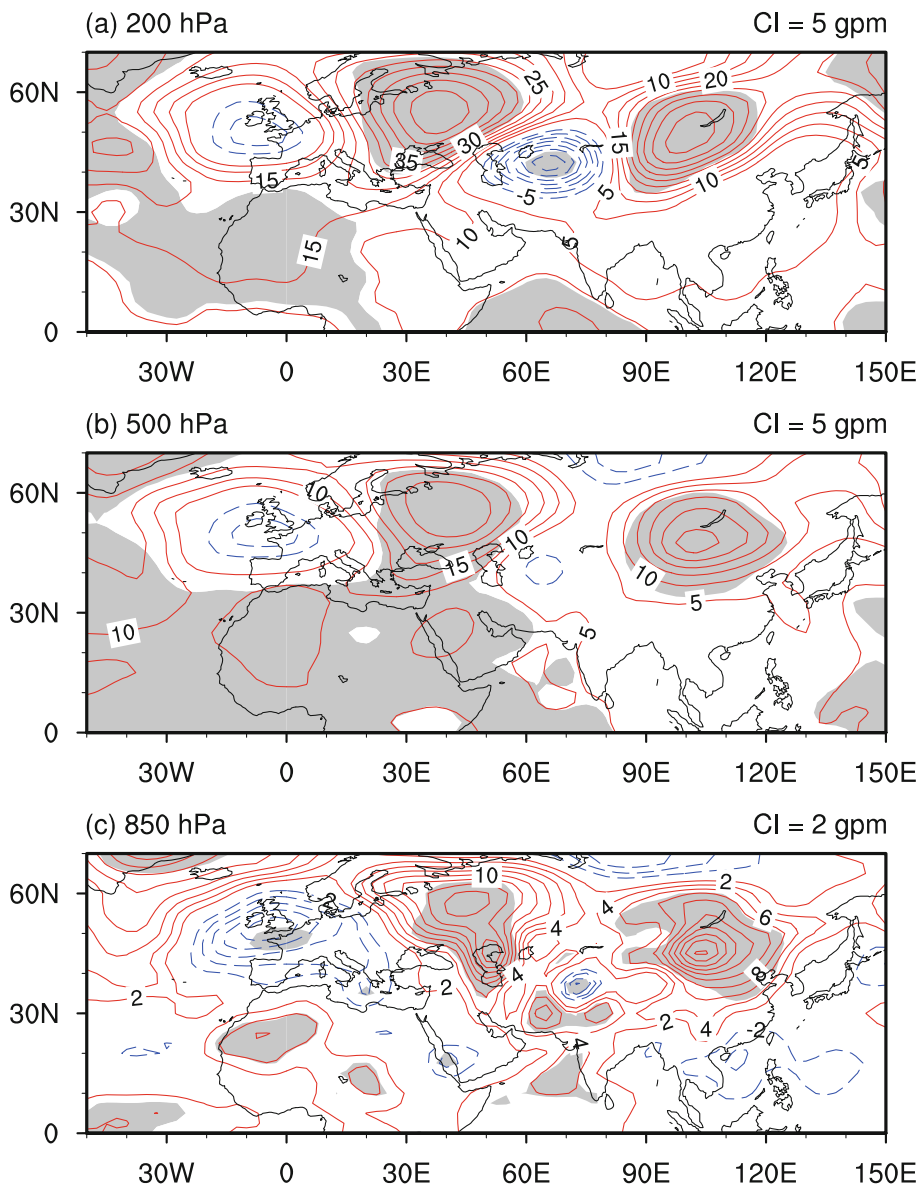

Fig. 9. (a) Differences in geopotential height at 200 hPa between 1999–2007 (T2) and 1971–2000 (TClim) (units: gpm). Gray shading indicates that the differences are significant above the 90% confidence, based on the Student's *t*-test. (b) As in (a), but for 500 hPa. (c) As in (a), but for 850 hPa. The red solid and blue dashed lines represent positive and negative values, respectively. Contour intervals are 5 gpm in (a, b) and 2 gpm in (c).
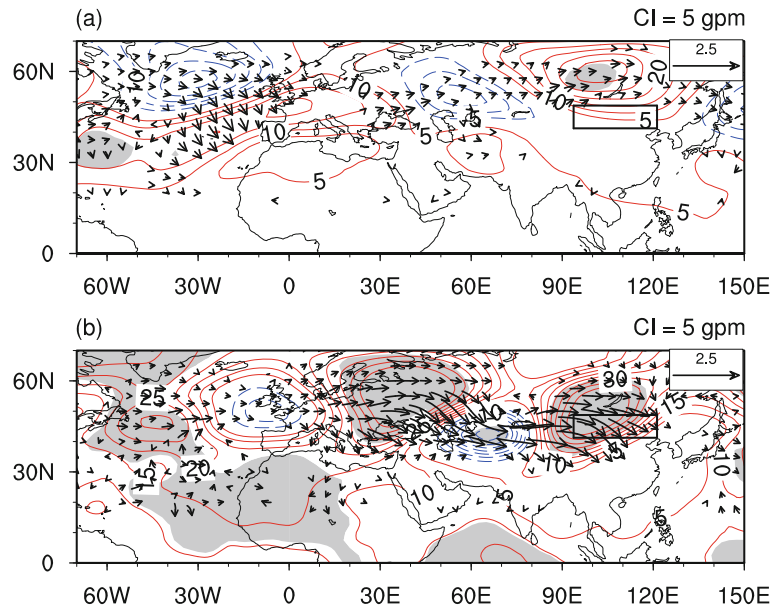
Fig. 10. (a) Difference in geopotential height (contours; units: gpm) and wave activity flux (vectors; units: $m^2\ s^{-2}$) at 200 hPa between T1 and the climatological mean state (TClim). Gray shading indicates that the difference in geopotential height is significant above the 90% confidence level, based on the Student's t-test. Vectors less than 0.01 are omitted. (b) As in (a), but between T2 and TClim. Contour intervals are 5 gpm.

the differences in zonal winds at 850 hPa between (22.5°–32.5°N, 110°–140°E) and (5°–15°N, 90°–130°E) (Wang and Fan, 1999); (2) $\mathrm{EASM_{ZHW}}$, defined as the zonal wind differences at 850 hPa and 200 hPa within (0°–10°N, 100°–130°E) (Zhu et al., 2000); and (3) $\mathrm{EASM_{HY}}$, defined as follows:

$$
\mathrm{EASM_{HY}} = \mathrm{Nor}\left[-\frac{0.25(z-\bar{z})\sin 45°}{\sin\phi_1} + \frac{0.50(z-\bar{z})\sin 45°}{\sin\phi_2} - \frac{0.25(z-\bar{z})\sin 45°}{\sin\phi_3} \right], \quad (13)
$$

where z, $\bar{z}$ and Nor denotes the summer mean geopotential height, the climatological mean geopotential height at 500 hPa and the normalization, respectively. ϕ_1, ϕ_2 and ϕ_3 are the corresponding latitudes of point (20°N, 125°E), point (40°N, 125°E) and point (60°N, 125°E), respectively. After applying a 9-yr running mean, the correlation coefficients between the intensity of the AIP's summer precipitation and the three monsoon indices, $\mathrm{EASM_{WF}}$, $\mathrm{EASM_{ZHW}}$, and $\mathrm{EASM_{HY}}$, are 0.419, 0.028 and 0.151, respectively, which are far from the 0.1 significance level. Thus, the weakening EASM may not be the driving factor of the interdecadal variation of rainfall over the AIP.

As for the excitation mechanism of the wave-like teleconnection pattern in the midlatitudes, many studies have documented the important role of SST anomalies (Li, 2004; Gu et al., 2009; Wu et al., 2010, 2011; Zhu et al., 2011; Zuo et al., 2013a). Figure 11 presents the difference in summer SST between T2 and TClim. Major positive anomalies are situated over the North Atlantic, the western Pacific and the

eastern Indian Ocean, while SST anomalies are negative over the tropical eastern Pacific. The anomalies over the North Atlantic and North Pacific are more significant than those over other regions. According to the study of Li (2004), the northwestern Atlantic SST anomalies may be a major contributor to a positive geopotential height anomaly over the Urals during early winter, by forcing a wave train–like anomaly chain. The tripole pattern of North Atlantic SST anomalies may influence the EASM via a barotropic wave-train pattern (Zuo et al., 2013a). In our study, the wave-like pattern propagates originating from Western Europe, which indicates that the wave source might be located in the North Atlantic. Hence, we mainly focus on the anomalies over the North Atlantic in the following analysis. Of course, the SST anomalies over the Pacific Ocean may also contribute to the change in summer precipitation over East China around the late 1990s, as indicated by Zhu et al. (2011) and Ueda et al. (2015).

To prove this assumption, we carry out two sensitivity experiments with AM2.1, as follows: (1) a control run with the climatological monthly mean SST derived from 30-yr monthly SSTs (1971–2000) as the boundary forcing (EXP_Ctrl); (2) a prescribed SST experiment the same as in the control run except that the boundary forcing is replaced with the climatological monthly mean plus observed SST differences in June, July and August between 1999–2007 and 1971–2000 in the North Atlantic within the domain (41°–49°N, 94°–124°E) (EXO_Pos); and (3) an experiment similar to EXO_Pos, except that the negative values of monthly mean SST differences in June, July and August between 1999–2007 and 1971–2000 in the North Atlantic are added to the clima-
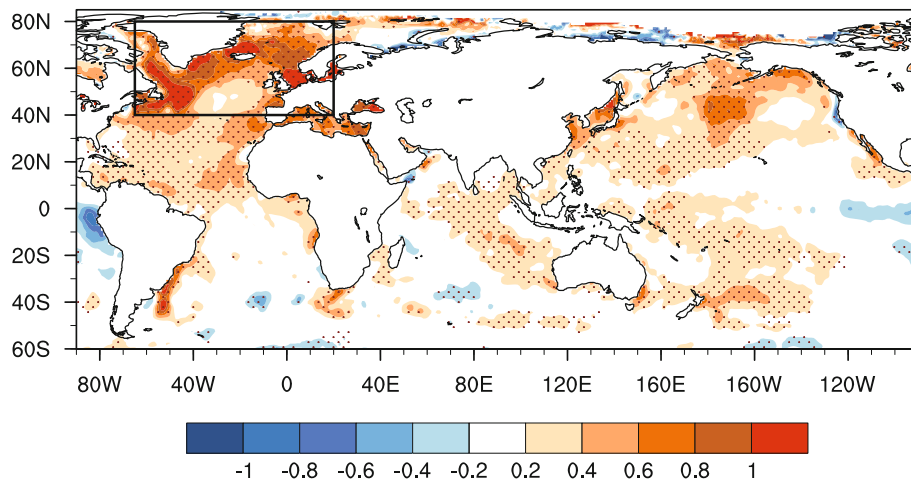
Fig. 11. Difference in SST (units: °C) between 1999–2007 and the climatological mean state. Contour intervals are 0.2°C and zero contour lines are omitted. The dotted areas indicate statistical significance at the 90% confidence level, based on the Student's *t*-test. The area within the black box here represents the North Atlantic region, the SST differences of which is added to the climatological mean SST as the boundary forcing of the sensitivity experiments.
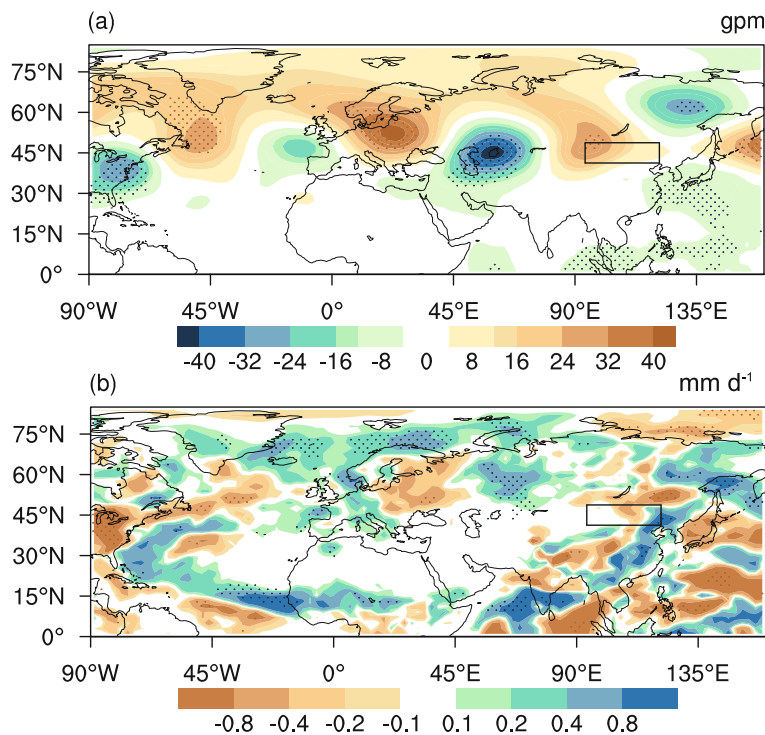

Fig. 12. (a) Difference in geopotential height at 200 hPa in the sensitivity experiment between EXP_Pos and EXP_Neg. (b) As in (a), but for the difference in precipitation in July and August. The dotted areas represent the 90% confidence level for the Student's *t*-test.

tological mean SST (EXP_Neg). The experiments are separately integrated for 20 years. Atmospheric forcings, such as greenhouse gases, aerosols and ozone, are fixed at 2000 levels. We mainly analyze the results in the last 10 years.

Figure 12 presents the differences in geopotential height at 200 hPa and summer precipitation between EXP_Pos and Exp_Neg. Clearly, Fig. 12a shows a quasi-zonal wave pat-

tern with positive centers over Eastern Europe and the AIP region, and negative centers over Central Asia. The pattern shown here is very similar to that shown in Fig. 9a. As for the precipitation field (Fig. 12b), the precipitation over Eastern Europe and the AIP region presents negative anomalies, while rainfall over the North Atlantic and Urals region shows positive anomalies, consistent with the teleconnection pat-

tern. Therefore, based on the observation data analyses and the GCM experiment results, it is suggested that the summer SST warming over the North Atlantic could excite the teleconnection pattern over Eurasia, resulting in the rainfall decrease over the AIP and worsening the drought condition there.

4.   Summary and discussion

In the AIP region, both the summer precipitation and annual precipitation are found to present an interdecadal shift around 1999. According to the differences in precipitation between 1971–2000 and 1999–2007, the whole AIP displays a robust decrease in precipitation during the latter period. Accompanying the rainfall decrease, sc-PDSI, SPEI and SPI all exhibit negative anomalies during 1999–2007, indicating an aggravated drought condition over the AIP. By analyzing the differences between SPEI and SPI, we find that the precipitation decrease and the rising temperature due to global warming are the main contributors to the development of drought.

A wave-like pattern over Eurasia in the atmospheric circulation anomalies is suggested as a possible reason for the interdecadal change in summer AIP rainfall. This wave-like teleconnection pattern shows wave propagation from Western Europe to the AIP, with a barotropic structure, which is much stronger during 1999–2007 than 1990–98. This teleconnection pattern is favorable for the formation of the anticyclone over the AIP in the latter period, resulting in the rainfall decrease and drought condition there. Further analysis also indicates that the weakening EASM seems not to be the driving factor of the interdecadal variation of rainfall over the AIP.

Further model simulations show that this teleconnection pattern in atmospheric circulation can be forced by the warming of summer SST over the North Atlantic. Observational results indicate that the strongest SST anomalies appear over the North Atlantic after the late 1990s. With the help of GCM sensitivity experiments, it is proven that the warming summer SST anomalies over the North Atlantic can force a wave-like teleconnection pattern over Eurasia, which is very similar to the observation. Also, the sensitivity experiments present a decrease in summer rainfall over the AIP for Atlantic warming. Regarding the cause of SST warming over the North Atlantic, many investigations have been performed that connect the warming anomalies with a hiatus in global surface warming during the first decade of the 21st century (Chen and Tung, 2014; Drijfhout et al., 2014; Trenberth et al., 2014). Given the multiple driving factors behind the North Atlantic warming, the mechanism remains a matter for further research.

REFERENCES

Anderson, J. L., and Coauthors, 2004: The new GFDL global atmosphere and land model AM2-LM2 Evaluation with prescribed SST simulations. *J. Climate*, **17**(24), 4641–4673.

Bai, Y. F., J. G. Wu, Q. Xing, Q. M. Pan, J. H. Huang, D. L. Yang, and X. G. Han, 2008: Primary production and rain use efficiency across a precipitation gradient on the Mongolia plateau. *Ecology*, **89**(8), 2140–2153, doi: 10.1890/07-0992.1.

Bao, G., Y. Liu, N. Liu, and H. W. Linderholm, 2015: Drought variability in eastern Mongolian Plateau and its linkages to the large-scale climate forcing. *Climate Dyn.*, **44**(3–4), 717–733, doi: 10.1007/s00382-014-2273-7.

Chen, G. S., and R. H. Huang, 2012: Excitation mechanisms of the teleconnection patterns affecting the July precipitation in Northwest China. *J. Climate*, **25**(22), 7834–7851, doi: 10.1175/jcli-d-11-00684.1.

Chen, H. P., and J. Q. Sun, 2015: Changes in drought characteristics over China using the standardized precipitation evapotranspiration index. *J. Climate*, **28**(13), 5430–5447, doi: 10.1175/jcli-d-14-00707.1.

Chen, M. Y., P. P. Xie, J. E. Janowiak, and P. A. Arkin, 2002: Global land precipitation: A 50-yr monthly analysis based on gauge observations. *Journal of Hydrometeorology*, **3**(3), 249–266, doi: 10.1175/1525-7541(2002)003<0249:GLPAYM>2.0. CO;2.

Chen, W., M. Takahashi, and H.–F. Graf, 2003: Interannual variations of stationary planetary wave activity in the northern winter troposphere and stratosphere and their relations to NAM and SST. *J. Geophys. Res.*, **108**(D24), 4797, doi: 10.1029/2003JD003834.

Chen, W., D. Q. Zhu, H. Z. Liu, and S. F. Sun, 2009: Land-air interaction over arid/semi-arid areas in China and its impact on the East Asian summer monsoon. Part I: Calibration of the Land Surface Model (BATS) using multicriteria methods. *Adv. Atmos. Sci.*, **26**(6), 1088–1098, doi: 10.1007/s00376-009-8187-3.

Chen, X. Y., and K.-K. Tung, 2014: Varying planetary heat sink led to global-warming slowdown and acceleration. *Science*, **345**(6199), 897–903, doi: 10.1126/science.1254937.

Delworth, T. L., and Coauthors, 2006: GFDL's CM2 global coupled climate models. Part I: Formulation and simulation characteristics. *J. Climate*, **19**(5), 643–674, doi: 10.1175/JCLI 3629.1.

Drijfhout, S. S., A. T. Blaker, S. A. Josey, A. J. G. Nurser, B. Sinha, and M. A. Balmaseda, 2014: Surface warming hiatus caused by increased heat uptake across multiple ocean basins. *Geophys. Res. Lett.*, **41**(22), 7868–7874, doi: 10.1002/2014 gl061456.

Endo, N., T. Kadota, J. Matsumoto, B. Ailikun, and T. Yasunari, 2006: Climatology and trends in summer precipitation char-

acteristics in Mongolia for the period 1960–98. *J. Meteor. Soc. Japan*, **84**(3), 543–551, doi: 10.2151/jmsj.84.543.

Gu, W., C. Y. Li, X. Wang, W. Zhou, and W. J. Li, 2009: Linkage between mei-yu precipitation and North Atlantic SST on the decadal timescale. *Adv. Atmos. Sci.*, **26**(1), 101–108, doi: 10.1007/s00376-009-0101-5. doi: 10.1007/s00376-009-0101-5

Huang, J., S. L. Sun, Y. Xue, and J. C. Zhang, 2015: Changing characteristics of precipitation during 1960–2012 in Inner Mongolia, northern China. *Meteor. Atmos. Phys.*, **127**(3), 257–271, doi: 10.1007/s00703-014-0363-z.

Huang, J. P., H. P. Yu, X. D. Guan, G. Y. Wang, and R. X. Guo, 2016: Accelerated dryland expansion under climate change. *Nature Climate Change*, **6**(2), 166–171, doi: 10.1038/nclimate2837.

Huang, R. H., Y. Liu, and T. Feng, 2013: Interdecadal change of summer precipitation over Eastern China around the late-1990s and associated circulation anomalies, internal dynamical causes. *Chinese Science Bulletin*, **58**(12), 1339–1349, doi: 10.1007/s11434-012-5545-9.

Kalnay, E., and Coauthors, 1996: The NCEP/NCAR 40-year reanalysis project. *Bull. Amer. Meteor. Soc.*, **77**(3), 437–471, doi: 10.1175/1520-0477(1996)077<0437:TNYRP>2.0.CO;2.

Lepage, Y., 1971: A combination of Wilcoxon's and Ansari-Bradley's statistics. *Biometrika*, **58**(1), 213–217, doi: 10.1093/biomet/58.1.213.

Li, S. L., 2004: Impact of northwest Atlantic SST anomalies on the circulation over the Ural Mountains during early winter. *J. Meteor. Soc. Japan*, **82**(4), 971–988, doi: 10.2151/jmsj.2004.971.

Lin, S.-J., 2004: A "Vertically Lagrangian" finite-volume dynamical core for global models. *Mon. Wea. Rev.*, **132**(10), 2293–2307, doi: 10.1175/1520-0493(2004)132<2293:AVLFDC>2.0.CO;2.

Liu, Y., G. Huang, and R. H. Huang, 2011: Inter-decadal variability of summer rainfall in Eastern China detected by the Lepage test. *Theor. Appl. Climatol.*, **106**(3–4), 481–488, doi: 10.1007/s00704-011-0442-8.

Liu, Y. Y., L. Wang, W. Zhou, and W. Chen, 2014: Three Eurasian teleconnection patterns: Spatial structures, temporal variability, and associated winter climate anomalies. *Climate Dyn.*, **42**(11–12), 2817–2839, doi: 10.1007/s00382-014-2163-z.

Ma, Z. G., and C. B. Fu, 2006: Some evidence of drying trend over northern China from 1951 to 2004. *Chinese Science Bulletin*, **51**(23), 2913–2925, doi: 10.1007/s11434-006-2159-0.

McKee, T. B., N. J. Doesken, and J. Kleist, 1993: The relationship of drought frequency and duration to time scales. *Preprints, 8th Conf. on Applied Climatology*, Anaheim, CA, Amer. Meteor. Soc., 179–184.

Milly, P. C. D., and A. B. Shmakin, 2002: Global modeling of land water and energy balances. Part I: The land dynamics (LaD) model. *Journal of Hydrometeorology*, **3**(3), 283–299, doi: 10.1175/1525-7541(2002)003<0283:GMOLWA>2.0.CO;2.

Mu, S. J., H. F. Yang, J. L. Li, Y. Z. Chen, C. C. Gang, W. Zhou, and W. M. Ju, 2013: Spatio-temporal dynamics of vegetation coverage and its relationship with climate factors in Inner Mongolia, China. *Journal of Geographical Sciences*, **23**(2), 231–246, doi: 10.1007/s11442-013-1006-x.

Myneni, R. B., F. G. Hall, P. J. Sellers, and A. L. Marshak, 1995: The interpretation of spectral vegetation indexes. *IEEE Trans. Geosci. Remote Sens.*, **33**(2), 481–486, doi: 10.1109/36.377948.

Nemani, R. R., C. D. Keeling, H. Hashimoto, W. M. Jolly, S. C. Piper, C. J. Tucker, R. B. Myneni, and S. W. Running, 2003: Climate-driven increases in global terrestrial net primary production from 1982 to 1999. *Science*, **300**(5625), 1560–1563, doi: 10.1126/science.1082750.

Palmer, W. C., 1965: Meteorological drought. Research Paper No 45, US Dept of Commerce, 58.

Peng, S. S., and Coauthors, 2013: Precipitation amount, seasonality and frequency regulate carbon cycling of a semi-arid grassland ecosystem in Inner Mongolia, China: A modeling analysis. *Agricultural and Forest Meteorology*, **178–179**, 46–55, doi: 10.1016/j.agrformet.2013.02.002.

Pettorelli, N., J. O. Vik, A. Mysterud, J. M. Gaillard, C. J. Tucker, and N. C. Stenseth, 2005: Using the satellite-derived NDVI to assess ecological responses to environmental change. *Trends in Ecology and Evolution*, **20**(9), 503–510, doi: 10.1016/j.tree. 2005.05.011.

Rayner, N. A., D. E. Parker, E. B. Horton, C. K. Folland, L. V. Alexander, D. P. Rowell, E. C. Kent, and A. Kaplan, 2003: Global analyses of sea surface temperature, sea ice, and night marine air temperature since the late nineteenth century. *J. Geophys. Res.*, **108**(D14), doi: 10.1029/2002JD002670.

Roerink, G. J., M. Menenti, W. Soepboer, and Z. Su, 2003: Assessment of climate impact on vegetation dynamics by using remote sensing. *Physics and Chemistry of the Earth, Parts A/B/C*, **28**(1–3), 103–109, doi: 10.1016/s1474-7065(03) 00011-1.

Running, S. W., 1990: Estimating terrestrial primary productivity by combining remote sensing and ecosystem simulation. *Remote Sensing of Biosphere Functioning*, R. J. Hobbs and H. A. Mooney, Eds., Springer-Verlag, 65–86, doi: 10.1007/978-1-4612-3302-2_4.

Sato, T., F. Kimura, and A. Kitoh, 2007: Projection of global warming onto regional precipitation over Mongolia using a regional climate model. *J. Hydrol.*, **333**(1), 144–154, doi: 10.1016/j.jhydrol.2006.07.023.

Takaya, K., and H. Nakamura, 2001: A formulation of a phase-independent wave-activity flux for stationary and migratory quasigeostrophic eddies on a zonally varying basic flow. *J. Atmos. Sci.*, **58**(6), 608–627, doi: 10.1175/1520-0469(2001)058<0608:AFOAPI>2.0.CO;2.

Tao, S. L., and Coauthors, 2015: Rapid loss of lakes on the Mongolian Plateau. *Proc. Natl. Acad. Sci. USA*, **112**(7), 2281–2286, doi: 10.1073/pnas.1411748112.

Trenberth, K. E., J. T. Fasullo, G. Branstator, and A. S. Phillips, 2014: Seasonal aspects of the recent pause in surface warming. *Nature Climate Change*, **4**(10), 911–916, doi: 10.1038/NCLIMATE2341.

Ueda, H., Y. Kamae, M. Hayasaki, A. Kitoh, S. Watanabe, Y. Miki, and A. Kumai, 2015: Combined effects of recent Pacific cooling and Indian Ocean warming on the Asian monsoon. *Nature Commun.*, **6**, 8854, doi: 10.1038/ncomms9854.

Van der Schirier, Barichivich, Briffa and Jones, 2013: A scPDSI-based global data set of dry and wet spells for 1901–2009. *J. Geophys. Res.*, **118**(10), 4025–4048, doi: 10.1002/jgrd.50355.

Vicente-Serrano, S. M., S. Beguería, and J. I. López-Moreno, 2010: A multiscalar drought index sensitive to global warming: The standardized precipitation evapotranspiration index. *J. Climate*, **23**(7), 1696–1718, doi: 10.1175/2009jcli2909.1.

Wang, B., and Z. Fan, 1999: Choice of south Asian summer monsoon indices. *Bull. Amer. Meteor. Soc.*, **80**, 629–638.

Wang, L., and W. Chen, 2014: A CMIP5 multimodel projection of future temperature, precipitation, and climatological drought in China. *International Journal of Climatology*, **34**(6), 2059–2078, doi: 10.1002/joc.3822.

Wang, L., W. Chen, and W. Zhou, 2014: Assessment of future drought in Southwest China based on CMIP5 multimodel projections. *Adv. Atmos. Sci.*, **31**(5), 1035–1050, doi: 10.1007/s00376-014-3223-3.

Wang, Z. W., P. M. Zhai, and H. T. Zhang, 2003: Variation of drought over northern China during 1950–2000. *Journal of Geographical Sciences*, **13**(4), 480–487, doi: 10.1007/BF02837887.

Wei, K., and L. Wang, 2013: Reexamination of the aridity conditions in arid Northwestern China for the last decade. *J. Climate*, **26**(23), 9594–9602, doi: 10.1175/jcli-d-12-00605.1.

Wells, N., S. Goddard, and M. J. Hayes, 2004: A self-calibrating Palmer drought serivity index. *J. Climate*, **17**, 2335–2351, doi: 10.1175/1520-0442(2004)017<2335:ASPDSI>2.0.CO;2.

Wu, R. G., S. Yang, S. Liu, L. Sun, Y. Lian, and Z. T. Gao, 2010: Changes in the relationship between Northeast China summer temperature and ENSO. *J. Geophys. Res.*, **115**(D21), doi: 10.1029/2010jd014422.

Wu, R. G., S. Yang, S. Liu, L. Sun, Y. Lian, and Z. T. Gao, 2011: Northeast China summer temperature and North Atlantic SST. *J. Geophys. Res.*, **116**(D16), doi: 10.1029/2011jd015779.

Xu, Z. Q., K. Fan, and H. J. Wang, 2015: Decadal variation of summer precipitation over China and associated atmospheric circulation after the late 1990s. *J. Climate*, **28**(10), 4086–4106, doi: 10.1175/jcli-d-14-00464.1.

Xue, X., W. Chen, D. Nath, and D. W. Zhou, 2015: Whether the decadal shift of South Asia High intensity around the late 1970s exists or not? *Theor. Appl. Climatol.*, **120**, 673–683, doi: 10.1007/s00704-014-1200-5.

Yamanaka, T., M. Tsujimura, D. Oyunbaatar, and G. Davaa, 2007: Isotopic variation of precipitation over eastern Mongolia and its implication for the atmospheric water cycle. *J. Hydrol.*, **333**(1), 21–34, doi: 10.1016/j.jhydrol.2006.07.022.

Yonetani, T., and G. J. McCabe, Jr., 1994: Abrupt changes in regional temperature in the conterminous United States, 1895–1989. *Climate Research*, **4**, 13–23, doi: 10.3354/cr004013.

Zhai, J. Q., B. D. Su, V. Krysanova, T. Vetter, C. Gao, and T. Jiang, 2010: Spatial variation and trends in PDSI and SPI indices and their relation to streamflow in 10 large regions of China. *J. Climate*, **23**(3), 649–663, doi: 10.1175/2009jcli2968.1.

Zhang, Y. S., T. Ohata, D. Q. Yang, and G. Davaa, 2004: Bias correction of daily precipitation measurements for Mongolia. *Hydrological Processes*, **18**(16), 2991–3005, doi: 10.1002/hyp.5745.

Zhou, L., R. K. Kaufmann, Y. Tian, R. B. Myneni, and C. J. Tucker 2003: Relation between interannual variations in satellite measures of northern forest greenness and climate between 1982 and 1999. *J. Geophys. Res.*, **108**(D1), ACL 3-1–ACL 3-16, doi: 10.1029/2002jd002510.

Zhu, C. W., J. H. He, and G. X. Wu, 2000: East Asian monsoon index and its interannual relationship with largescale thermal dynamic circulation. *Acta Meteorologica Sinica*, **58**, 391–402. (in Chinese)

Zhu, L. K., and J. J. Meng, 2010: Spatiotemporal variation of precipitation in the central Inner Mongolia in recent 43 years. *Arid Zone Research*, **27**(4), 536–544. (in Chinese)

Zhu, Y. L., H. J. Wang, W. Zhou, and J. H. Ma, 2011: Recent changes in the summer precipitation pattern in East China and the background circulation. *Climate Dyn.*, **36**(7–8), 1463–1473, doi: 10.1007/s00382-010-0852-9.

Zhu, Y. L., T. Wang, and H. J. Wang, 2016: Relative contribution of the anthropogenic forcing and natural variability to the interdecadal shift of climate during the late 1970s and 1990s. *Science Bulletin*, **61**(5), 416–424, doi: 10.1007/s11434-016-1012-3.

Zou, X. K., P. M. Zhai, and Q. Zhang, 2005: Variations in droughts over China: 1951–2003. *Geophys. Res. Lett.*, **32**(4), doi: 10.1029/2004GL021853.

Zuo, Z. Y., R. H. Zhang, and P. Zhao, 2011: The relation of vegetation over the Tibetan Plateau to rainfall in China during the boreal summer. *Climate Dyn.*, **36**(5–6), 1207–1219, doi: 10.1007/s00382-010-0863-6.

Zuo, J. Q., W. J. Li, C. H. Sun, L. Xu, and H.-L. Ren, 2013a: Impact of the North Atlantic sea surface temperature tripole on the East Asian summer monsoon. *Adv. Atmos. Sci.*, **30**(4), 1173–1186, doi: 10.1007/s00376-012-2125-5.

Zuo, Z. Y., S. Yang, R. H. Zhang, P. P. Jiang, L. Zhang, and F. Wang, 2013b: Long-term variations of broad-scale Asian summer monsoon circulation and possible causes. *J. Climate*, **26**(22), 8947–8961, doi: 10.1175/jcli-d-12-00691.1.